

Aeromechanics Modelling of Tiltrotor Aircraft

Wesley Appleton, Antonio Filippone & Nicholas Bojdo
 The University of Manchester, UK
 wesley.appleton@manchester.ac.uk

Abstract

A numerical investigation into the influence of different aerodynamic interaction models on the trim behaviour of tiltrotor aircraft was undertaken. The study simulated the entire conversion corridor and compared a baseline case, with no interaction accounted for, with simulations that included different interaction models: rotor-induced download on the wing; wing downwash at the tailplane; and the rotor wake effect at the tailplane. The entire conversion corridor was simulated using a reduced-order blade element/strip theory framework. The influence of the interactions models was compared for the trimmed pitch attitude and control stick position. The most important interaction to account for was the wing downwash at the tailplane. This interaction was found to have a pronounced effect on the trim state at all operating points and influenced the predicted conversion corridor boundaries.

The unique feature of tiltrotor aircraft is their conversion corridor that bounds the flight speed as a function of the rotor tilt. The capability of tilting the rotors while maintaining controllable flight expands the traditional flight envelopes of rotorcraft and aircraft to form a single, wider envelope. These aircraft therefore deliver the hover and low-speed operability of the helicopter, coupled with the range, speed and altitude advantages of turboprop aircraft. The conversion corridor is characterised by the wing stall at the lower speed boundary and the installed engine power and the control limits at the higher speed boundary. Figure 1 illustrates a typical conversion corridor. The corridor is broad when the ro-

tors are vertical, with the flight speed ranging from hover through to the power speed limit at the upper boundary. After the rotors are tilted, the corridor begins to narrow when the rotors cannot singularly provide the required aircraft lift and propulsive forces. Furthermore, as the aircraft weight increases, both the stall speed and required power increase, narrowing the corridor and effectively reducing the flight envelope.

The wake of the lateral-tandem rotors can have a significant and adverse interaction with airframe in hover and low-speed forward helicopter mode. The rotor downwash immerses the wing and creates a rotor-induced download on the airframe. The incidence of the rotor wake relative to the wing causes a bluff-body stall with large separation². This download force increases the required rotor thrust and power, with the download equating to approximately 10% - 15% of the thrust. The implication of the download on the aircraft negatively affects the vertical take-off payload capability³. Furthermore, the rotor wake interacts with the empennage of the airframe. The exact interaction with the empennage is dependent on the operating condition and em-

Copyright Statement

The authors confirm that they, and/or their company or organization, hold copyright on all of the original material included in this paper. The authors also confirm that they have obtained permission, from the copyright holder of any third party material included in this paper, to publish it as part of their paper. The authors confirm that they give permission, or have obtained permission from the copyright holder of this paper, for the publication and distribution of this paper as part of the ERF proceedings or as individual offprints from the proceedings and for inclusion in a freely accessible web-based repository.

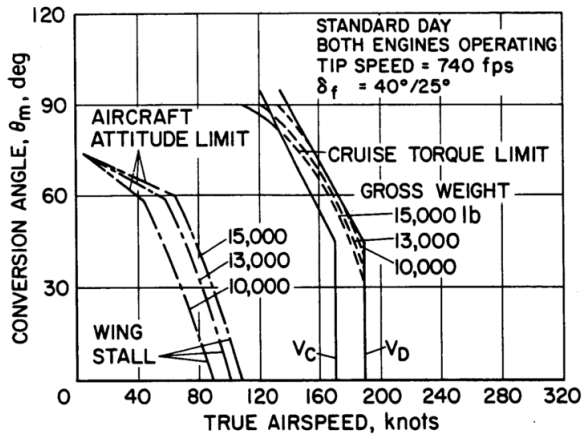


Figure 1: The conversion corridor for the XV-15 research tiltrotor, taken from Maisel¹. The conversion angle θ_m is measured from the aircraft longitudinal axis, δ_f is the flap/ flaperon setting, V_C is the cruise speed and V_D is the dive speed.

penance configuration, which is not generally available in the literature with empirically derived models or experimental data. However, the rotor wake interaction with the empennage is documented for the H-tail configuration found on the XV-15 tiltrotor. In helicopter mode, the vorticity in the wake rolls up downstream towards the empennage. This creates an upwash at the tailplane, changing to a downwash as the rotors are tilted further towards aeroplane mode^{4,5}. Additionally, the deflected wake of the wing also imposes a downwash at the tailplane, representing another source of wake interaction with the airframe.

Due to the large operating envelope of tiltrotor aircraft, reduced-order methods are used to efficiently model and explore the aircraft behaviour over a wide-range of operating points, i.e. rotor tilt angle, flight speed, gross weight, cg position, flap setting. Several aeromechanics models exist in literature^{6,7,8}, however, the implications of incorporating different aerodynamic interactions is not considered. Appleton et al.⁹ used reduced-order models to predict the conversion corridor of the XV-15, neglecting any aerodynamic interaction. The results captured the general trends through flight transi-

tion, with the largest discrepancy observed during the early conversion angles from helicopter mode.

This study numerically investigates the effects of the rotor and wing wakes, both individually and combined, on the aircraft trim behaviour and predicted flight speed boundaries. The purpose of the study is to understand the influence of the interactions in trimmed flight and identify if any of these interactions are necessary to consider from a preliminary, design viability and assessment standpoint. A generic tiltrotor model is first constructed and configured to the XV-15 literature model from Harendra et al.⁷, owing to the large amount of required geometric and aerodynamic data. The baseline simulation, including no interference modelling, is then validated against the full simulation model. Thereafter, the effects of the rotor and wing wakes are studied individually and simultaneously.

1. Tiltrotor Simulation Model

The simulation model is constructed for generic tiltrotor configurations. The aircraft is discretised into the major aerodynamic components: fuselage; rotors; wing; and empennage. The empennage is modelled as a single component owing to the various empennage configurations observed on current tiltrotor aircraft. This discretisation forms the basic framework of the simulation model with the total loads on the aircraft subsequently found by summing the individual component loads in a body-fixed frame. The loads are calculated successively in the downstream direction. The total generic load on the aircraft F is then

$$(1) \quad F = F_F + F_R + F_W + F_E,$$

where the subscript letters denote the component references.

The rotary-wing and fixed-wing aerodynamic models are based on an individual element model, i.e. blade element or strip theory. Each element is

assumed to operate in a closed two-dimensional flowfield independent from adjacent elements. Spanwise flow effects are neglected in both the rotary-wing and fixed-wing models.

The aerodynamic data for the XV-15 blade was modelled from similar NACA 64-series aerofoils using the experimental data of Abbott et al.¹⁰. The original aerofoils of the XV-15 blade are detailed by Felker et al.¹¹ and were used to select similar NACA 64-series aerofoils in terms of the design lift coefficient and thickness-to-chord ratio. The post-stall lift was modelled using the empirically derived model of Spera¹². The post-stall drag of all the aerofoil sections was modelled from the experimental results of a NACA 63A012 aerofoil by Dadone¹³. This approximation was used to improve the predicted power correlation of the rotor model at all operating points.

1.1. Rotary-Wing Aerodynamics

The rotor thrust and drag (in-plane force) coefficients C_T and C_H are defined normal to hub plane and rearwards in the hub plane. The coefficients are dimensionless on $\pi\rho\Omega^2 R^4$, where ρ is the freestream air density, Ω is the shaft speed and R is the blade radius. The rotor torque coefficient C_Q is defined positive against the shaft motion and dimensionless on $\pi\rho\Omega^2 R^5$. The blade twist and chord distributions were taken from Harendra et al.⁷.

The rotary-wing analysis is performed in a disc-wind system, i.e. the tip-path-plane axes with the in-plane disc axis aligned with the resultant in-plane velocity. The gimbal flapping is derived relative to the nonrotating hub plane. The disc-wind axes are obtained through successive rotations about the longitudinal and lateral flap angles β_c and β_s and the disc sideslip angle Δ . Let the linear velocity of the rotor in the hub axes, dimensionless on ΩR , be

$$(2) \quad \boldsymbol{\nu} = \nu_x \mathbf{i}^h + \nu_y \mathbf{j}^h + \nu_z \mathbf{k}^h,$$

where the unit vectors \mathbf{i}^h , \mathbf{j}^h and \mathbf{k}^h point normal

to the hub plane and starboard and forwards in the hub plane. If the disc is flapped by the angles β_c and β_s , then the disc sideslip angle Δ is

$$(3) \quad \Delta = \arcsin(\mu_y/\mu),$$

where

$$(4) \quad \begin{aligned} \mu_y &= \nu_x \beta_s + \nu_y, \\ \mu_z &= \nu_z - \nu_x \beta_c, \\ \mu &= \sqrt{\mu_y^2 + \mu_z^2}. \end{aligned}$$

1.1.1. Blade Aerodynamics

Blade element theory is well covered in many rotary-wing textbooks and will not be presented in-depth here. Only an overview, covering the conventions used, are detailed. The dimensionless blade forces in the perpendicular and tangential directions, \hat{F}_P and \hat{F}_T , positive in the conventional thrust and drag directions, are:

$$(5) \quad \begin{aligned} \hat{F}_P &= \frac{1}{2\pi} \int_e^1 \hat{c} \hat{V} (\hat{V}_T C_l - \hat{V}_P C_d) d\hat{r}, \\ \hat{F}_T &= \frac{1}{2\pi} \int_e^1 \hat{c} \hat{V} (\hat{V}_T C_d + \hat{V}_P C_l) d\hat{r}, \end{aligned}$$

where e is the root cut-off fraction, \hat{c} and \hat{r} are the normalised chord and spanwise location, \hat{V} is the resultant velocity and \hat{V}_T and \hat{V}_P are the tangential and perpendicular velocity components:

$$(6) \quad \begin{aligned} \hat{V}_P &= \lambda + \hat{r} \frac{d\bar{\beta}_s}{d\psi} \sin \bar{\psi} + \left(\mu \beta_p + \hat{r} \frac{d\bar{\beta}_c}{d\psi} \right) \cos \bar{\psi}, \\ \hat{V}_T &= \hat{r} + \mu \sin \bar{\psi}, \end{aligned}$$

where λ is the inflow ratio, $d\bar{\beta}_c/d\psi$ and $d\bar{\beta}_s/d\psi$ are the gimbal flap rates resolved into the disc-wind axes, β_p is the blade precone angle and $\bar{\psi}$ is the azimuth-wind angle

$$(7) \quad \bar{\psi} = \psi + \Delta.$$

The blade forces are resolved into the nonrotating hub axes and summed over B blades to give the net

thrust and in-plane forces.

The blade element forces also give rise to aerodynamic moments out-of-plane and in-plane, $d\hat{M}_\beta$ and $d\hat{M}_\xi$:

$$(8) \quad \begin{aligned} \hat{M}_\beta &= \int_e^1 \hat{r} d\hat{F}_P, \\ \hat{M}_\xi &= \int_e^1 \hat{r} d\hat{F}_T, \end{aligned}$$

where the out-of-plane moment and in-plane moment are taken positive upwards and lagwise.

The loss of lift towards the blade tip was modelled using an effective lifting radius R_e approximated from Sissingh¹⁴:

$$(9) \quad \frac{R_e}{R} = 1 - \frac{\sqrt{2C_T}}{B},$$

The rotor thrust was calculated for hover at design gross weight, giving $R_e/R = 0.953$. This value was then assumed to be constant at all operating conditions. Outboard of the effective span, the lift was reduced to zero and the blade set to produce only profile drag.

1.1.2. Gimbal Dynamics

The flapping equations of motion for the gimballed rotor were derived by considering the inertial and aerodynamic loads on a blade element. The derivation follows that presented by Padfield¹⁵, where the rotor is treated as a single dynamic structure rather than an articulated blade approach. The blade element out-of-plane moment is integrated along the blade span, resolved into the pitch and roll axes, and summed over B blades to give the coupled equations of motion in the nonrotating hub frame. A hub spring is also included, giving the equations of motion with respect to the azimuth angle:

$$(10) \quad \begin{aligned} \frac{d^2\beta_s}{d\psi^2} - 2\frac{d\beta_c}{d\psi} + \frac{2K}{BI\Omega^2}\beta_s &= \frac{M_s}{I\Omega^2}, \\ \frac{d^2\beta_c}{d\psi^2} + 2\frac{d\beta_s}{d\psi} + \frac{2K}{BI\Omega^2}\beta_c &= \frac{M_c}{I\Omega^2}, \end{aligned}$$

where K is the spring stiffness, I is the out-of-plane moment of inertia of a blade, Ω is the shaft speed and M_c and M_s are the multi-blade flap moments:

$$(11) \quad \begin{aligned} M_s &= \frac{2}{B} \sum_{i=1}^B (M_\beta \sin \psi)_i, \\ M_c &= \frac{2}{B} \sum_{i=1}^B (M_\beta \cos \psi)_i. \end{aligned}$$

The aerodynamic flap moment from blade element theory is

$$(12) \quad M_\beta = \pi\rho\Omega^2 R^5 \hat{M}_\beta.$$

The gimbal equations of motion were solved as a system of first-order differential equations and integrated using a second-order Runge-Kutta method until the transient motion had decayed and the quasi-steady, periodic rotor flapping was obtained.

As the gimbal flaps, the pitch links are pulled-up and pushed-down creating an effective cyclic pitch¹⁵. This effective cyclic pitch provides aerodynamic damping stabilising the flapping motion. The blade pitch of a gimballed rotor can then be written as

$$(13) \quad \begin{aligned} \theta &= \theta_{tw} + \theta_0 + (\bar{\theta}_c - \bar{\beta}_s - \bar{\beta}_c \tan \delta_3) \cos \bar{\psi} \\ &+ (\bar{\theta}_s + \bar{\beta}_c - \bar{\beta}_s \tan \delta_3) \sin \bar{\psi}, \end{aligned}$$

where θ_{tw} is the built-in twist, θ_0 is the collective pitch, θ_s and θ_c are the longitudinal and lateral cyclic pitches, δ_3 is the pitch-flap coupling and β_c and β_s are the effective cyclic pitches from the gimbal flapping. The overbar implies the quantities are transformed into the disc-wind axes through the disc sideslip angle.

1.1.3. Induced Flow

Owing to the large design space and operating conditions of tiltrotor aircraft, a computationally efficient induced flow model was used. The induced flow was modelled using the dynamic inflow theory

of Peters and HaQuang¹⁶ where the induced inflow is prescribed in a first-harmonic Fourier series

$$(14) \lambda_i(\hat{r}, \bar{\psi}) = \lambda_0 + \hat{r}\lambda_s \sin \bar{\psi} + \hat{r}\lambda_c \cos \bar{\psi},$$

where λ_i is the induced flow ratio at a spatial point on the disc, λ_0 is the mean component through the disc, λ_s and λ_c are the lateral and longitudinal gradients and $\bar{\psi}$ is the disc-wind azimuth angle. The induced flow states are dynamically related to the aerodynamic thrust, pitch and roll moments on the rotorhead through the governing state-space system:

$$(15) [\tau] \frac{d\lambda_i}{d\psi} + \lambda_i = [L]F,$$

where $[\tau]$ is the time constant matrix associated with the dynamic lag of the system and $[L]$ is the gain matrix. The forcing and induced flow state vectors, F and λ_i , are:

$$(16) \begin{aligned} \lambda_i &= \{\lambda_0 \ \lambda_s \ \lambda_c\}^T, \\ F &= \{\bar{C}_T \ -\bar{C}_L \ -\bar{C}_M\}^T, \end{aligned}$$

where \bar{C}_L and \bar{C}_M are the aerodynamic roll and pitch moments and the overbar indicates disc-wind quantities. The matrices are not repeated for brevity as they are widely found in literature. The induced flow states are combined with the gimbal states and integrated through time until a periodic solution is obtained. The quasi-steady rotor loads are then rotated through the rotor tilt angle into the body-fixed frame for substitution into the equations of motion.

1.2. Fixed-Wing Aerodynamics

The fixed-wing aerodynamics are calculated in a wing-fixed frame, accounting for arbitrary pitch, dihedral and sweep angles. The wing is modelled as a pair of semi-span wings with the geometric angles referenced to the starboard side. The wing is first assumed to span laterally from the aircraft centreline to starboard. The wing is first rotated through

the dihedral angle Γ , positive upwards. The wing is then swept through the angle Λ , positive wings aft, using a shear transformation rather than a rotation. This was adopted as the industry standard is to have the wing element chord line parallel to the aircraft centreline¹⁷. Finally, the wing is rotated through the pitch angle θ , positive leading-edge up, about the span axis. The small angle approximation for the dihedral and sweep angles is not made allowing for an arbitrary wing to be spatially orientated, e.g. a vertical tail is a mapped through a 90 deg dihedral angle. The pitch angle is assumed to be small that the small angle approximation is made.

Denote the aerodynamic velocity components in the body-fixed frame along the forward and vertical axes, normalised by ΩR , as \hat{u}_a and \hat{w}_a . The velocity components in the chordwise and chord-normal directions of a wing element, \hat{V}_C and \hat{V}_N , are then

$$(17) \begin{aligned} \hat{V}_C &= \hat{u}_a - \theta \hat{w}_a \cos \Gamma, \\ \hat{V}_N &= \theta \hat{u}_a + \hat{w}_a \cos \Gamma. \end{aligned}$$

The element angle of attack α is then

$$(18) \alpha = \arctan(\hat{V}_N/\hat{V}_C),$$

and is used to linearly interpolate an incompressible lookup table for the lift, drag and moment coefficients, C_l , C_d and C_{m_0} . The chordwise and chord-normal forces $d\hat{F}_C$ and $d\hat{F}_N$, defined positive in the lift and drag directions, are

$$(19) \begin{aligned} d\hat{F}_C &= \frac{1}{2\pi} \hat{c}\hat{V}^2 (C_d \cos \alpha - C_l \sin \alpha) d\hat{y}, \\ d\hat{F}_N &= \frac{1}{2\pi} \hat{c}\hat{V}^2 (C_l \cos \alpha + C_d \sin \alpha) d\hat{y}, \end{aligned}$$

where \hat{c} and \hat{y} are the normalised chord and span and \hat{V} is the resultant velocity. The forward and vertical forces of the aircraft are obtained by rotating the element loads back to the body-fixed axes and

integrating along the semi-span:

$$(20) \quad \begin{aligned} \hat{X} &= - \int_0^{\hat{b}} (d\hat{F}_C + \theta d\hat{F}_N) , \\ \hat{Z} &= \int_0^{\hat{b}} (\theta \cos \Gamma d\hat{F}_C - \cos \Gamma d\hat{F}_N) , \end{aligned}$$

where \hat{b} is the normalised wing span. The pitching moment developed by the semi-wing is calculated from

$$(21) \quad \hat{M} = \int_0^{\hat{b}} (\hat{l} d\hat{Z} - \hat{h} d\hat{X} + d\hat{M}_0 \cos \Gamma) ,$$

where \hat{l} and \hat{h} are normalised longitudinal and vertical positions of the strip relative to the cg, measured positive aft and above:

$$(22) \quad \begin{aligned} \hat{l} &= \hat{l}_0 + \hat{y} \sin \Lambda , \\ \hat{h} &= \hat{h}_0 + \hat{y} \sin \Gamma , \end{aligned}$$

with \hat{l}_0 and \hat{h}_0 being the coordinates of the wing root quarter-chord relative to the cg and $d\hat{M}_0$ being the element pitching moment:

$$(23) \quad d\hat{M}_0 = \frac{1}{2\pi} \hat{c}^2 \hat{V}^2 C_{m_0} d\hat{y} .$$

For a wing on the port side of the aircraft, the spanwise ordinate is negative and the spatial position and orientation are obtained by using dihedral and sweep angles of opposite sign to the starboard wing. Control surface deflections are defined positive trailing-edge down on the starboard wing when its viewed spanning laterally starboard.

2. Aerodynamic Interference

The flowfield around a tiltrotor aircraft is extremely complex with the rotor and wing wakes potentially creating significant interactions with the airframe. The two main sources of aerodynamic interaction out-of-ground effect are the rotor-induced download on the wing and the wakes of both the rotor and wing at the tailplane.

The download was accounted for using methods similar to Dreier¹⁸ and Makofski and Menkirk¹⁹: the rotor wake was modelled as a contracted streamtube with the freestream and rotor wake velocities implemented into a strip model. In this work, the velocity of the rotor wake, defined parallel to the shaft axis, was related to the mean induced flow ratio using the expression developed by McCormick²⁰:

$$(24) \quad \lambda_w = \left(1 + \frac{d}{\sqrt{1+d^2}} \right) \lambda_0 ,$$

where λ_w is the wake velocity, d is the distance from the wing element to the rotor and λ_0 is the mean induced flow. The skew angle of the rotor wake from the shaft axis is then

$$(25) \quad \chi = \arctan \left(\frac{\nu_z}{|\nu_x + \lambda_w|} \right) .$$

The rotor wake velocity is added to the freestream velocity of the spanwise strip if the quarter-chord is bounded by the skew angles at the front and rear of the disc at the same spanwise position. The body-frame aerodynamic velocity components at the control point, denoted with a subscript a , are then

$$(26) \quad \begin{aligned} \hat{u}_a &= \hat{u} + \lambda_w \sin \tau , \\ \hat{w}_a &= \hat{w} - \lambda_w \cos \tau , \end{aligned}$$

where τ is the rotor angle measured from the aircraft vertical.

The rotor and wing wake effects at the empennage were modelled using the interaction models from Harendra et al.⁷: the rotor wake adds an incremental velocity component to the freestream velocity of the aircraft and the wing wake deflects this resultant flow through the downwash angle as a function of wing angle of attack, flap setting and rotor tilt angle. From Harendra et al., the rotor wash at the

tailplane was approximated from the polynomial

$$(27) \quad \frac{\lambda_t}{\lambda_0} = h_0 + h_1\tau + (h_2 + h_3\tau)H, \\ H = \left(\frac{\hat{u} - h_4 + h_5\tau}{h_4} \right)^2,$$

where λ_t is the induced flow at the tailplane, λ_0 is mean induced flow and the h constants have the values:

$$h_0 = -0.5838, \\ h_1 = 0.0116, \\ h_2 = 0.5967, \\ h_3 = 0.0024, \\ h_4 = 51.5/\Omega R, \\ h_5 = -2.2519.$$

The induced flow at the tailplane is then resolved into the body axes and added to the freestream velocity. Finally, this resultant flow is rotated through the downwash angle, linearly interpolated from the data in Figure 2, to give the effective angle of attack at the tailplane.

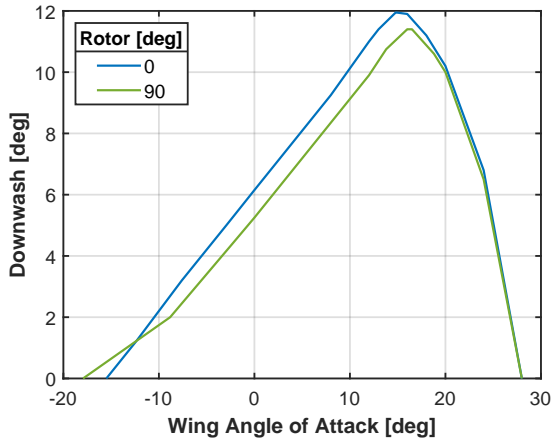


Figure 2: Downwash angle as a function of the wing angle of attack. Data from Harendra et al.⁷. The rotors are vertical at 0 deg and horizontal at 90 deg.

3. Conversion Corridor

The aircraft was trimmed in steady level flight at rotor angles from vertical (0 deg) to horizontal (90 deg) in 15 deg intervals, at flight speed increments of 10 kn. The trim solution was found by solving for the angle of attack, collective pitch, longitudinal cyclic pitch and elevator input required to hold a given condition, i.e. flight speed, flight path angle, gross weight and cg position. To create a determined system of trim equations, the longitudinal pitch controls (longitudinal cyclic pitch θ_s and elevator deflection η) were related to the stick displacement δ_{l0} . The trim state of the aircraft is therefore uniquely dependent on the relation between the two pitch controls. Following the model of Harendra et al., the longitudinal cyclic pitch was washed-out sinusoidally with the rotor tilt angle and the elevator control was kept constant:

$$(28) \quad \frac{d\theta_s}{d\delta_{l0}} = A \cos \tau, \\ \frac{d\eta}{d\delta_{l0}} = B,$$

where A and B are the maximum deflection values.

The convergence of the trim equations is largely dependent on the initial guess, particularly when using nonlinear aerodynamic lookup tables. To improve the convergence of the trim solution if no trim history was available, the collective pitch was approximated from linear aerodynamics to give a specified blade loading C_T/σ :

$$(29) \quad \frac{C_T(\theta_0)}{\sigma} = 0.07 \cos \tau + 0.03.$$

The blade loading values were selected as an approximation to the operating value as a function of the rotor angle. The conversion corridor was simulated for the XV-15 aircraft at 5900 kg gross weight at the aft cg limit. The constraints imposed on the

trim state were:

$$(30) \quad \begin{aligned} |\beta| &\leq 12 \text{ deg} , \\ |\delta_{I_o}| &\leq 1 , \\ C_{P_{\max}} &\leq 0.0015 , \end{aligned}$$

where β is the amplitude of the flapping and $C_{P_{\max}}$ is the normalised installed power of a single engine. Furthermore, the longitudinal cyclic pitch and elevator deflections were

$$(31) \quad \begin{aligned} A &= -10 \text{ deg} , \\ B &= 20 \text{ deg} . \end{aligned}$$

4. Results and Discussions

4.1. Baseline Simulation

The baseline simulation case, not including any interaction models was first validated against the simulation model of Harendra et al.⁷ (plotted as discrete triangles in all plots herein). Figure 3 shows the correlation of the predicted pitch attitude in trimmed level flight as a function of the flight speed and rotor tilt angle. The predicted trim attitude shows good correlation to the simulation model, particularly with the rotors vertical and near aeroplane mode. The baseline model tended to overpredict the lower speed boundary for rotor tilt angles of 30 deg, 60 deg and 90 deg. The constraining parameter at these rotor angles was found to be the required aft stick being larger than the permitted value. The stick required in trimmed level flight is presented in Figure 4 where a large discrepancy between the baseline and simulation models is observed. In most cases, the required stick to trim is underpredicted. At a rotor tilt of 30 deg, the low speed trim solution tends to pitch the aircraft nose-up and flap the rotor disc backwards, attempting to align the thrust vector against the weight vector due to the low dynamic pressure over the wing. However, the required flap angle is larger than the permitted limit of $|\beta| \leq 12$ deg and thus trim is not

feasible until the flight speed reaches 80 kn. Wing stall is encountered at a fuselage angle of attack of approximately 11 deg. The results of the baseline simulation case near aeroplane mode show that trim was not possible above this value for rotor tilt angles towards aeroplane mode. Overall, the predicted trim states matched those of Harendra et al. fairly well over the entire domain, thus validating the baseline tiltrotor model.

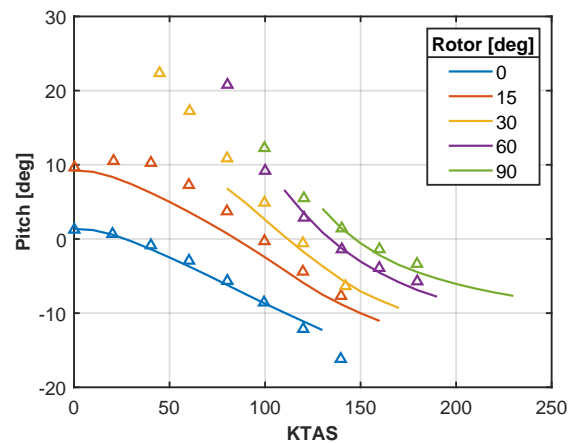


Figure 3: Trimmed pitch attitude for the baseline simulation case.

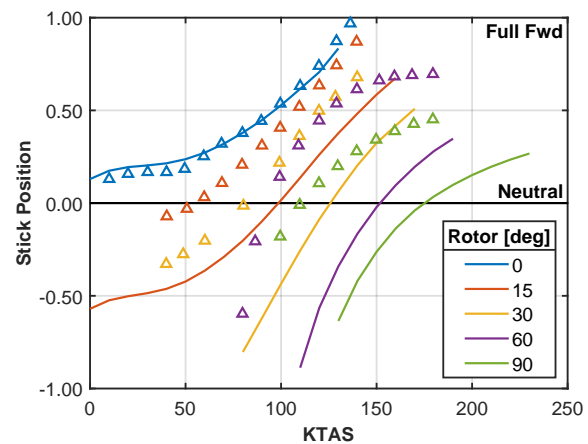


Figure 4: Trimmed stick position for the baseline simulation case.

4.2. Rotor-Induced Download

Figures 5 and 6 show the influence of the download model on the trimmed pitch angle and stick posi-

tions. The influence of the download model was almost negligibly small throughout the trim sweep. This was due to the relatively small distance between the cg and wing strips, resulting in a small moment arm. A more pronounced effect would be expected with a forward cg, resulting in a more nose-down attitude and aft stick travel to compensate against the rotor-induced nose-up wing moment. The minimum flight speed in aeroplane mode was found to decrease by 10 kn from the increased dynamic pressure acting over a large area of the wing. The larger dynamic pressure required a smaller angle of attack to produce the same lift, requiring less aft stick to trim.

The influence of the rotor-induced download was best assessed in terms of the increase in required power. Figure 7 shows the ratio of the power with and without the inclusion of the download model. For the rotor in hover, the download resulted in approximately an 8% increase in the required power. The largest increase in required power was 14% in low-speed helicopter mode up to a flight speed of 40 kn. This was due to the larger aerodynamic velocities over the wing (sum of the freestream velocity and mean induced flow) and the resultant negative incidence at the wing sections. Above a flight speed of 40 kn, the downwash is decreased as the skew angle of the wake from the shaft axis increases causing the inboard wing sections to lie outside the rotor wake. For the case of the rotors tilted by 15 deg, the reduced effectiveness of the wing due to the rotor downwash and the trade-off between the wing and rotor forces at higher speeds results in a subsequent increase of the rotor power. These results are not validation to a highly simplified method of approximating the download effects, however, they do agree qualitatively with the download effect disappearing in helicopter mode around 60 kn due to the convection of the wake²¹. The importance of the download model would only be significant if the installed power is sufficiently low such that the required hover and low-speed power is close to the

available power.

As the rotors are tilted forwards in front of the wing, an increased area of the wing is immersed in the large-diameter rotor wake. Consequently, a small increase in rotor power was found through conversion mode at higher flight speeds due to an increase of the wing induced drag to compensate for the decrease in effective angle of attack. In aeroplane mode, the induced flow component is parallel to the forward axis of the aircraft and thus slightly increases the dynamic pressure and reduces the angle of attack. This was reflected as a small decrease in required power due to the reduced induced drag component.

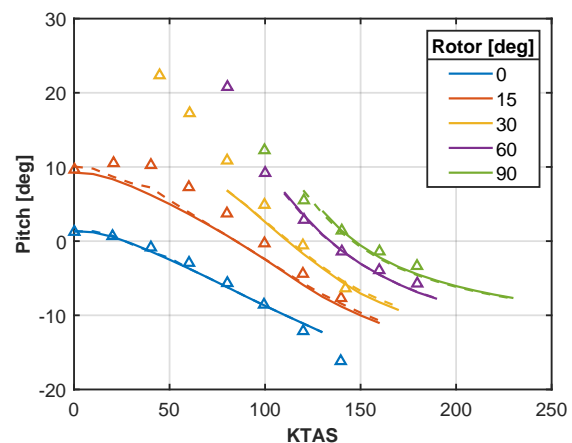


Figure 5: Effect of the download model on the trimmed pitch angle, presented as dashed lines.

4.3. Wing Wake at the Empennage

The trim sweep results with the inclusion of the wing downwash at the tailplane are presented in Figures 8 and 9. It is evident that the inclusion of a wing downwash model has a significant effect on the trim behaviour. The downwash effect on the trimmed pitch attitude was most pronounced from hover to a flight speed of approximately 120 kn in helicopter and early conversion mode. Conversely, the largest influence on trimmed stick position was found from a flight speed of approximately 80 kn onwards affecting the rotor after 30 deg forward

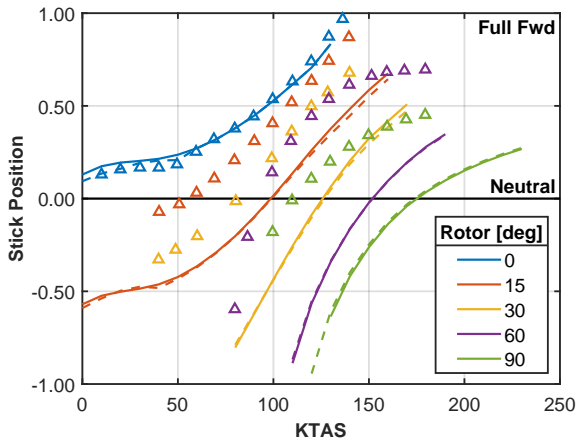


Figure 6: Effect of the download model on the trim stick position, presented in dashed lines.

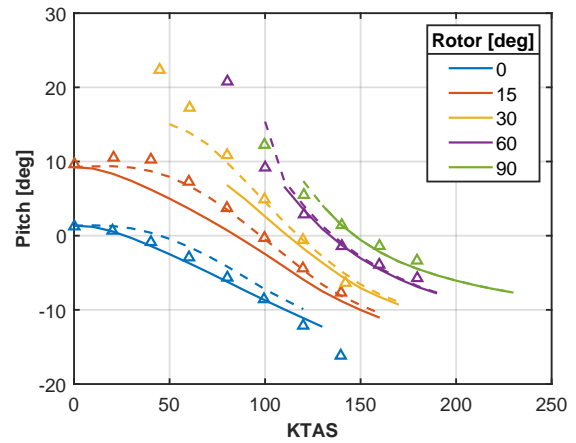


Figure 8: Trimmed pitch attitude for the baseline simulation case against those with a wing downwash model included, presented as dashed lines.

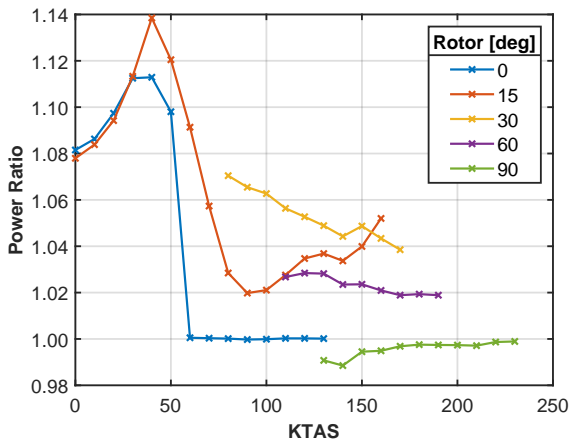


Figure 7: Ratio of the predicted power using the download model to the baseline model, presented as a function of airspeed and rotor angle.

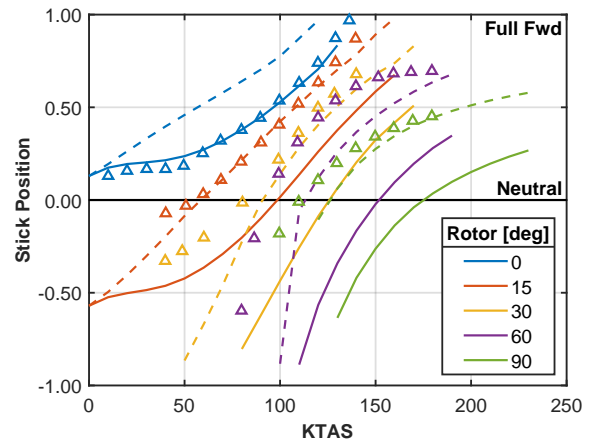


Figure 9: Trimmed stick position for the baseline simulation case against those with a wing downwash model included, presented as dashed lines.

tilt. Figures 10 and 11 show the difference in the trimmed pitch and stick compared to the baseline case, illustrating the effect of the wing downwash was to increase the aircraft pitch angle and migrate the trimmed stick position forward.

The effect of the wing downwash decreases the tailplane lift since the effective angle of attack α_e is decreased:

$$(32) \quad \alpha_e = \alpha - \varepsilon,$$

where α is the freestream angle of attack and ε is the downwash angle from the wing wake. Conse-

quently, a larger pitch-up moment is created and must be counter-acted to trim. The magnitude of the downwash in trimmed flight is shown in Figure 12. It is observed that due to the large flap/ flap-eron settings employed to improve the low-speed wing lift capability, the created downwash angles are substantial.

Figure 13 shows the net empennage lift in the baseline case and the wing downwash case for the rotors vertical and tilted forward by 15 deg. For the baseline case from after hover to a flight speed of 50 kn, the tailplane applied a small nose-down

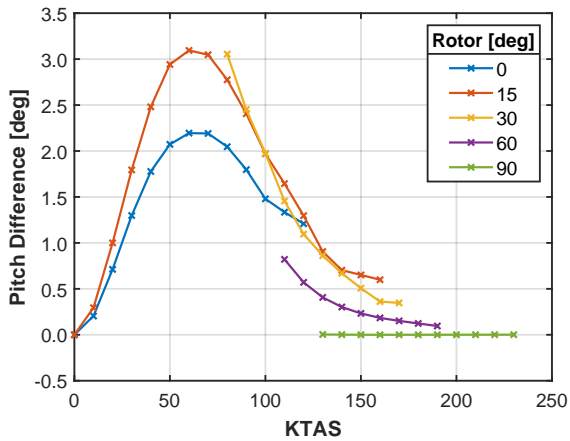


Figure 10: Difference in trimmed pitch angle when the wing downwash model is included.

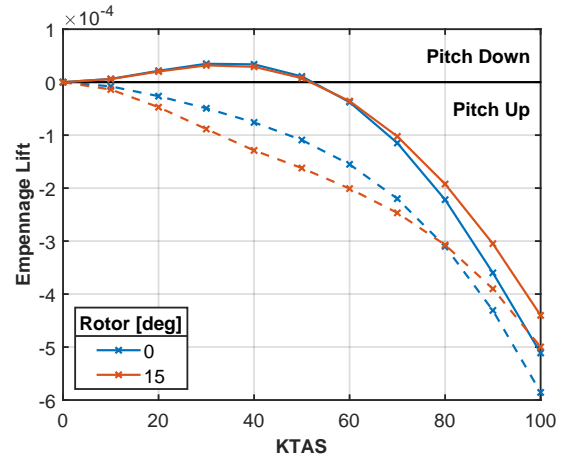


Figure 13: Net dimensionless lift produced by the tailplane in the baseline case and with the downwash model, presented as dashed lines.

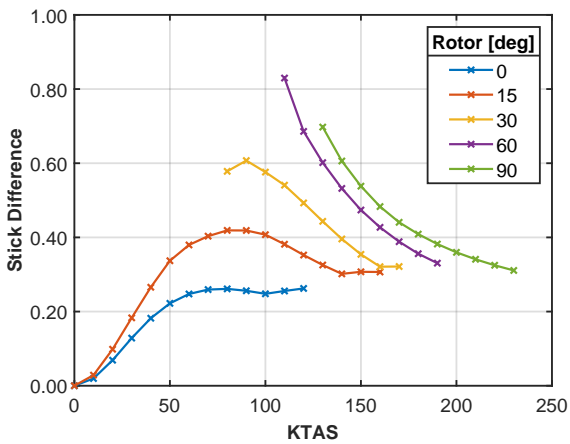


Figure 11: Difference in the trimmed stick position when the wing downwash model is included.

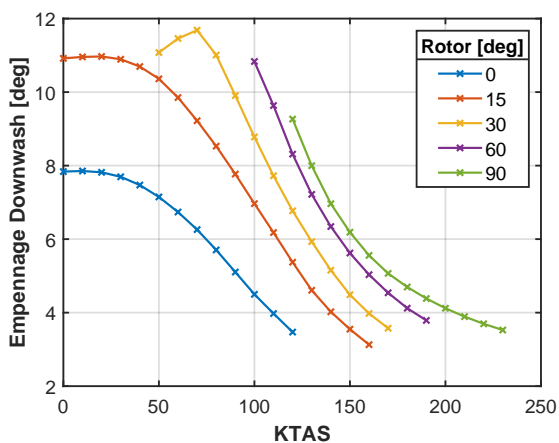


Figure 12: Downwash angle at the tailplane due to the wing in trimmed level flight.

moment caused by the forward stick position and the applied elevator deflection. This was not found when the downwash was included. At low speed, the additional pitch-down moment was provided by the rotor flapping. The stick is moved forward to increase the forward flap angle β_c , increasing the nose-down moment from the rotor thrust. However, the rotor also provides most of the airframe lift at these operating conditions. Therefore, the aircraft simultaneously pitches nose-up to realign the orientation of the thrust vector against the weight vector. As the aircraft is pitched up, there is a larger 1/rev aerodynamic flap moment from the higher advance ratio (freestream velocity in the hub plane), causing the disc to flap backwards. This requires further longitudinal cyclic to flap the disc forwards, helping to provide the pitch-down moment. The additional forward travel of the stick reduces the maximum trimmed flight speed obtainable with the rotors at 0 deg, decreasing it by 10 kn compared to the baseline case. As the flight speed increases further and more control authority is gained from the elevator, the differences between the two simulation cases begins to reduce.

For the rotor in helicopter and conversion mode at rotor angles of 15 deg and 30 deg, the wing downwash model significantly improves the corre-

lation to the simulation values from Harendra et al.. From simple lifting-line theory, the downwash at the tailplane is proportional to the lift coefficient of the wing²², and hence the angle of attack. With the rotors tilted forward from the vertical, at low speed the trimmed pitch attitude tends to be nose-up to orientate the thrust vector against the weight vector. In doing so, the wing angle of attack is increased along with the downwash, up to stall. At this pitch-up attitude, the tendency of the tailplane is to pitch the aircraft nose-down, more than if the downwash was included. To compensate for the nose-down moment, the stick is moved aft to flap the disc backwards towards the vertical to give a nose-up moment from the rotor. When the wing downwash is included, the tail moment is naturally decreased and the elevator authority increased. The required stick position consequently migrates forward with less flap-back required. As a result, the lower speed boundary at 30 deg rotor tilt is reduced by 30 kn, from 80 kn to 50 kn.

The wing downwash model does not change the trimmed pitch angle significantly through the flight speed range at rotor angles past 60 deg. However, the lower speed boundary is decreased by 10 kn in both cases. This was due to the reduced effective angle of attack at the tailplane, reducing the nose-down moment and increasing the control authority of the elevator, evidenced by Figure 9. For the rotor at 60 deg tilt flying at 110 kn, the stick position travels from near full aft to being approximately neutral, a change of 41.5% of the total permitted stick travel.

4.4. Rotor Wake at the Empennage

The effect of including only the rotor wash at the tailplane on the trimmed pitch and stick are shown in Figures 14 and 15. The rotor wake effect in aeroplane mode was not found to be significant. In helicopter mode, as the flight speed increased to around 40 kn, the rotor vortices roll-up above the tailplane creating an upwash, with the dynamic

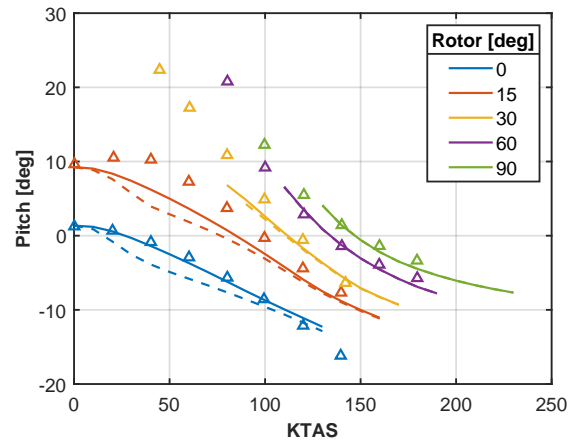


Figure 14: Trimmed pitch attitude for the baseline simulation case against those with a rotor wake model at the empennage included, presented as dashed lines

pressure approaching twice the freestream value⁴. As the airspeed increased further, the rolled-up wake moved downward relative to the tailplane, decreasing the net upwash, but the upwash still being present. The effect of the rotor wake upwash at the tailplane is contrary to the downwash effect. The increased effective angle of attack produces a larger nose-down moment that, at low speed, requires an increase in flap-back of the rotor created by moving the stick aft. The new orientation of the rotor thrust vector is accompanied by a change in pitch attitude, in this case nose down, to realign the new thrust vector towards the weight vector.

The upwash phenomenon at the tailplane demonstrates a clear stick reversal, i.e. the gradient of the stick with respect to increasing flight speed shows a negative gradient in helicopter and conversion mode up to 40 kn. Whilst this does not have a direct impact on the predicted flight speed boundaries, it is important when considering the control and stability of the aircraft. The only change in flight speed limit was found for 30 deg rotor tilt, with the lower speed boundary increasing by 10 kn. This was due to the increased aft stick required to trim exceeding the control inputs available to the rotor and elevator.

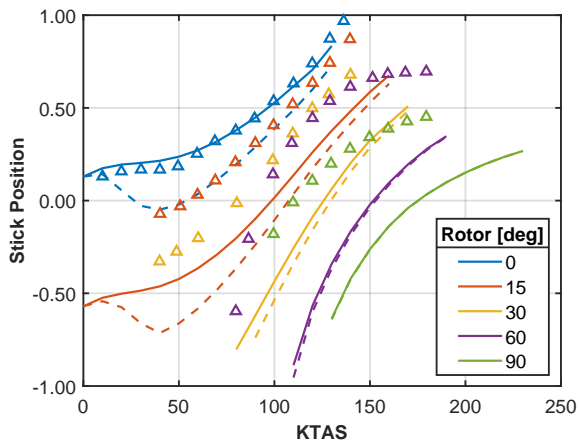


Figure 15: Trimmed stick position for the baseline simulation case against those with a rotor wake model at the empennage included, presented as dashed lines.

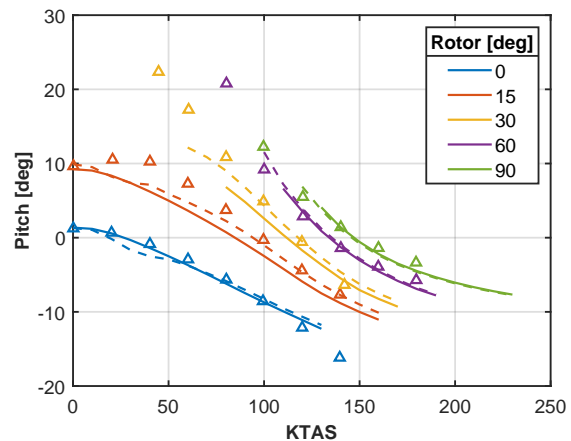


Figure 16: Trimmed pitch attitude for the baseline simulation case against those including the rotor and wing wake models, presented as dashed lines.

4.5. Combined Aerodynamic Interference

The combined effects of the interference models on the trim behaviour are shown in Figures 16 and 17. The upwash due to the roll-up of the rotor wake on the trimmed pitch attitude is clearly exhibited in helicopter and conversion mode up to 40 kn. However, its magnitude is reduced considerable when the wing downwash is included. A shallow stick reversal remains when the rotors are vertical but disappears when the rotors are tilted forward to 15 deg, the latter being caused by the increased wing downwash from the required pitch-up attitude. Furthermore, the wing downwash expands the lower speed boundary of the corridor for rotor angles past 15 deg due to the decreased tail moment and improved elevator control authority.

5. Conclusions

A numerical study has been used to assess the implications of aerodynamic interference models on the predicted conversion corridor of tiltrotor aircraft. The study has investigated the influence of the models primarily on the trimmed pitch angle and the stick position in steady level flight. The baseline case with no interference models showed reason-

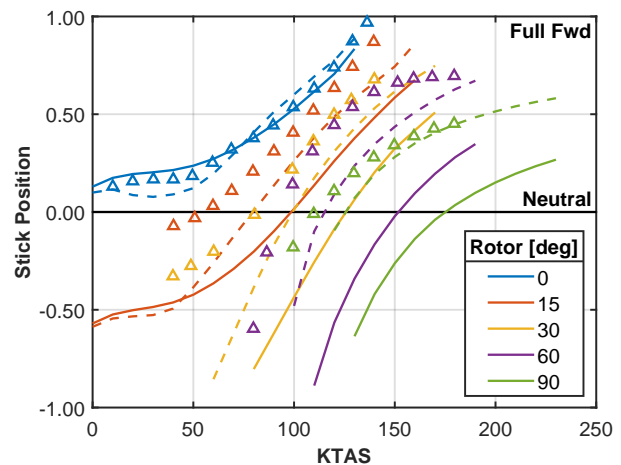


Figure 17: Trimmed stick position for the baseline simulation case against those including the rotor and wing wake models, presented as dashed lines.

able correlation to the simulation results of Harendra et al.⁷. In particular, the trimmed pitch correlated well with the rotors vertical and near aeroplane mode, however, underpredicted the pitch at low-speed forward flight with the rotors tilted at 15 deg and 30 deg. The general trend of the baseline trimmed stick position was aft of the simulation results by Harendra et al., implying a greater pitch-up control moment was required.

The rotor-induced downwash was not found to have a significant effect on the aircraft trim behaviour throughout all operating points considered.

The increase in required power due to the download was found to be approximately 8% in hover and increased up to 14% at around 40 kn. Thereafter, the increased skew angle of the wake reduced the immersed wing area, reducing the download. Through conversion mode, the tilt of the rotor disc immerses the wing in the rotor wake, felt as a downwash, and subsequently requires more rotor power to overcome its adverse effects. The added induced flow component in aeroplane mode was found to decrease the minimum flight speed by 10 kn. The importance of the download model would only likely be significant if the excess power in hover and low speed is small.

The main effect of the rotor wake at the empennage in helicopter mode was to produce an upwash at the tailplane. Its influence on the trim behaviour past 15 deg forward tilt was found to be almost negligible. The rotor wake did not significantly change the flight speed boundaries, except increasing the low-speed boundary at 30 deg forward tilt as a result of the additional aft stick exceeding the model limitations.

The inclusion of the downwash model at the tailplane showed significant differences from the baseline case and generally improved the correlation against the simulation results of Harendra et al.. The downwash model reduced the effective angle of attack at the tailplane creating a larger nose-up moment. This was compensated for by increasing the forward flapping of the disc creating a larger nose-down moment and migrating the stick position forward. The new inclination of the thrust vector then required the aircraft to pitch nose-up to realign the thrust vector against the weight vector. The minimum flight speed was decreased for rotor tilts between 30 deg and 90 deg, with the largest decrease of 30 kn found at 30 deg of rotor tilt. For rotor tilts of 60 deg and 90 deg, the lower speed boundary was decreased by 10 kn. When the rotors were vertical, the increased nose-up moment caused by the downwash was compensated with additional

forward stick, resulting in a 10 kn decrease of the maximum trimmed flight speed. The influence of the wing downwash at the tailplane was found to have the most significant effect on the predicted trim states, as well as increasing the trimmable flight domain. As such, a suitable downwash model, either analytical, empirical or experimental, should be employed in prediction of the conversion corridor boundaries at an initial or preliminary design stage.

Acknowledgements

This research was partly funded by the Aircraft Research Association (ARA Ltd.), Bedford, UK. Part-funding from the Vertical Lift Network (VLN), under EPSRC Grant EP/M018164/1, is also acknowledged.

References

- [1] M. Maisel. Tilt Rotor Research Aircraft Familiarization Document. *NASA TM X-62 407*, 1975.
- [2] W. McCroskey, P. Spalart, G. Laub, M. Maisel, and B. Maskew. Airloads on Bluff Bodies, with Application to the Rotor-Induced Downloads on Tilt-Rotor Aircraft. *NASA TM 84401*, 1983.
- [3] F. Felker. A Review of Tilt Rotor Download Research. In *14th European Rotorcraft Forum*, 1988.
- [4] R. Marr, K. Sambell, and G. Neal. V/STOL Tilt Rotor Study. Volume 6: Hover, Low Speed and Conversion Tests of a Tilt Rotor Aeroelastic Model. *NASA CR 114615*, 1973.
- [5] R. Marr, D. Ford, and S. Ferguson. Analysis of the Wind Tunnel Test of a Tilt Rotor Power Force Model. *NASA CR 137529*, 1974.
- [6] S. Diaz, E. Mouterde, and A. Desopper. Performance Code for Take-Off and Landing Tilt-Rotor Procedures Study. In *30th European Rotorcraft Forum*, Marseille, 2004.
- [7] P. Harendra, M. Joglekar, T. Gaffey, and R. Marr. V/STOL Tilt Rotor Study - Volume 5: A Mathematical Model For Real Time Flight Simulation

- of the Bell Model 301 Tilt Rotor Research Aircraft. *NASA CR 114614*, 1973.
- [8] S. Ferguson. A Mathematical Model for Real Time Flight Simulation of a Generic Tilt-Rotor Aircraft. *NASA CR 166563*, 1988.
- [9] W. Appleton, A. Filippone, and N. Bojdo. Low-Order Aeromechanics of Tilt-Rotor Helicopters. In *44th European Rotorcraft Forum*, 2018.
- [10] I. Abbott, A. von Doenhoff, and L. Stivers Jr. Summary of Aerofoil Data. *NACA TR 824*, 1945.
- [11] F. Felker, M. Betzina, and D. Signor. Performance and Loads Data from a Hover Test of a Full-Scale XV-15 Rotor. *NASA TM 86833*, 1985.
- [12] D. Spera. Models of Lift and Drag Coefficients of Stalled and Unstalled Airfoils in Wind Turbines and Wind Tunnels. *NASA CR 215434*, 2008.
- [13] L. Dadone. Helicopter Design DATCOM. Volume 1 - Airfoils. Technical report, 1976.
- [14] G. Sissingh. Contribution to the Aerodynamics of Rotating-Wing Aircraft: Part 2. *NACA TM 990*, 1941.
- [15] G. Padfield. *Helicopter Flight Dynamics: Including a Treatment of Tiltrotor Aircraft*. Wiley, 3rd edition, 2018. ISBN 9781119401056.
- [16] D. Peters and N. HaQuang. Dynamic Inflow for Practical Applications. *Journal of the American Helicopter Society*, 1988.
- [17] R. Vos and S. Farokhi. *Introduction to Transonic Aerodynamics*. Springer, 2015. ISBN 978-94-017-9746-7.
- [18] M. Dreier. *Introduction to Helicopter and Tiltrotor Flight Simulation*. AIAA, 2007. ISBN 1563478730.
- [19] R. Makofski and G. Menkick. Investigation of Vertical Drag and Periodic Airloads acting on Flat Panels in a Rotor Slipstream. *NACA TN 3900*, 1956.
- [20] B. McCormick. *Aerodynamics of V/STOL Flight*. Academic Press, 1967. ISBN 0-486-40460-9.
- [21] A. Desopper, O. Heuzé, V. Routhieau, S. Baehrel, G. Roth, and W. von Grünhagen. Study of the Low Speed Characteristics of a Tiltrotor. In *28th European Rotorcraft Forum*, 2002.
- [22] E. Houghton and P. Carpenter. *Aerodynamics for Engineering Students*. Butterworth-Heinemann, 5th edition, 2003. ISBN 0-7506-5111-3.